References and Notes

1. S. C. Solomon, R. L. McNutt Jr., R. E. Gold, D. L. Domingue, *Space Sci. Rev.* **131**, 3 (2007).
2. Materials and methods are available as supporting material on *Science* Online.
3. M. T. Zuber *et al.*, *Science* **336**, 217 (2012); 10.1126/science.1218805.
4. P. M. Muller, W. L. Sjogren, *Science* **161**, 680 (1968).
5. D. E. Smith *et al.*, *J. Geophys. Res.* **98**, 20871 (1993).
6. D. E. Smith *et al.*, *Icarus* **209**, 88 (2010).
7. J. D. Anderson, J. Palguta, G. Schubert, Abstract P41A-1572, paper presented at the American Geophysical Union Fall Meeting, San Francisco, CA, 5 to 9 December 2011.
8. L. R. Nittler *et al.*, *Science* **333**, 1847 (2011).
9. L. R. Nittler *et al.*, Abstract 142-3, paper presented at the Geological Society of America Annual Meeting, Minneapolis, MN, 9 to 12 October 2011.
10. B. Charlier, T. L. Grove, M. T. Zuber, *Lunar Planet. Sci.* **43**, abstract 1400 (2012).
11. M. T. Zuber *et al.*, *Science* **321**, 77 (2008).
12. F. Nimmo, T. R. Watters, *Geophys. Res. Lett.* **31**, L02701 (2004).
13. G. A. Neumann, M. T. Zuber, D. E. Smith, F. G. Lemoine, *J. Geophys. Res.* **101** (E7), 16841 (1996).
14. M. T. Zuber *et al.*, *Science* **287**, 1788 (2000).
15. J. W. Head *et al.*, *Science* **333**, 1853 (2011).
16. R. G. Strom, G. Neukum, in *Mercury,* F. Villas, C. R. Chapman, M. S. Matthews, Eds. (Univ. of Arizona Press, Tucson, 1988), pp. 363–373.
17. P. J. McGovern *et al.*, *J. Geophys. Res.* **109**, E07007 (2004).
18. J.-L. Margot, S. J. Peale, R. F. Jurgens, M. A. Slade, I. V. Holin, *Science* **316**, 710 (2007).
19. S. J. Peale, *Nature* **262**, 765 (1976).
20. S. J. Peale, R. J. Phillips, S. C. Solomon, D. E. Smith, M. T. Zuber, *Meteorit. Planet. Sci.* **37**, 1269 (2002).
21. M. Yseboodt, J.-L. Margot, *Icarus* **181**, 327 (2006).
22. J.-L. Margot, S. Padovan, S. J. Peale, S. C. Solomon, Abstract P41A-1573, paper presented at the American Geophysical Union Fall Meeting, San Francisco, CA, 5 to 9 December 2011.
23. S. A. Hauck II, S. C. Solomon, D. A. Smith, *Geophys. Res. Lett.* **34**, L18201 (2007).
24. V. Malavergne, M. J. Toplis, S. Berthet, J. Jones, *Icarus* **206**, 199 (2010).
25. G. Morard, T. Katsura, *Geochim. Cosmochim. Acta* **74**, 3659 (2010).
26. U. R. Christensen, *Nature* **444**, 1056 (2006).
27. S. A. Hauck II, A. J. Dombard, R. J. Phillips, S. C. Solomon, *Earth Planet. Sci. Lett.* **222**, 713 (2004).
28. M. T. Zuber *et al.*, *Icarus* **209**, 88 (2010).
29. W. M. Kaula, *Theory of Satellite Geodesy* (Blaisdell, Waltham, MA, 1966).

Acknowledgments: The MESSENGER project is supported by the NASA Discovery Program under contracts NAS5-97271 to The Johns Hopkins University Applied Physics Laboratory and NASW-00002 to the Carnegie Institution of Washington. We acknowledge the contributions of the MESSENGER spacecraft team and the radio science and MLA instrument teams in acquiring the observations used herein. We are also grateful to three anonymous reviewers for comments that improved the manuscript.

Supporting Online Material

www.sciencemag.org/cgi/content/full/science.1218809/DC1
Materials and Methods
Figs. S1 to S7
References (*30*–*37*)

6 January 2012; accepted 5 March 2012
Published online 21 March 2012;
10.1126/science.1218809

Topography of the Northern Hemisphere of Mercury from MESSENGER Laser Altimetry

Maria T. Zuber,[1]* David E. Smith,[1] Roger J. Phillips,[2] Sean C. Solomon,[3] Gregory A. Neumann,[4] Steven A. Hauck II,[5] Stanton J. Peale,[6] Olivier S. Barnouin,[7] James W. Head,[8] Catherine L. Johnson,[9] Frank G. Lemoine,[4] Erwan Mazarico,[1,4] Xiaoli Sun,[4] Mark H. Torrence,[4,10] Andrew M. Freed,[11] Christian Klimczak,[3] Jean-Luc Margot,[12] Jürgen Oberst,[13] Mark E. Perry,[7] Ralph L. McNutt Jr.,[7] Jeffrey A. Balcerski,[5] Nathalie Michel,[5] Matthieu J. Talpe,[1] Di Yang[1]

Laser altimetry by the MESSENGER spacecraft has yielded a topographic model of the northern hemisphere of Mercury. The dynamic range of elevations is considerably smaller than those of Mars or the Moon. The most prominent feature is an extensive lowland at high northern latitudes that hosts the volcanic northern plains. Within this lowland is a broad topographic rise that experienced uplift after plains emplacement. The interior of the 1500-km-diameter Caloris impact basin has been modified so that part of the basin floor now stands higher than the rim. The elevated portion of the floor of Caloris appears to be part of a quasi-linear rise that extends for approximately half the planetary circumference at mid-latitudes. Collectively, these features imply that long-wavelength changes to Mercury's topography occurred after the earliest phases of the planet's geological history.

The topography of a planet provides fundamental information about its internal structure and geological and thermal evolution. Ranging observations made from orbit by the Mercury Laser Altimeter (MLA) (*1*) on the MErcury Surface, Space ENvironment, GEochemistry, and Ranging (MESSENGER) (*2*) spacecraft have provided a precise, geodetically referenced topographic model of the northern hemisphere of the planet as well as a characterization of slopes and surface roughness over a range of spatial scales.

From MESSENGER's eccentric, near-polar orbit (*2*), the MLA (*3*) illuminates surface areas averaging between 15 and 100 m in diameter, spaced ~400 m apart along the spacecraft ground track. The range from the spacecraft to the surface is converted to a measurement of radius from the planet's center of mass via the determination of MESSENGER's orbit. Radius is then converted to topography (Fig. 1A) by subtracting the radius of the gravitational equipotential or geoid obtained from Doppler tracking of MESSENGER (*4*). The radial precision of individual measurements is <1 m, and the accuracy with respect to Mercury's center of mass is better than 20 m (Table 1). MLA can successfully range at distances up to 1500 km from Mercury's surface when operating at nadir, and from ~1000 km at angles up to 40° from the vertical (*5*). As of 2 December 2011, more than 4.3 million independent measurements of surface elevation had been obtained.

Elevations in Mercury's northern hemisphere exhibit an approximately symmetric, unimodal hypsometric distribution and a dynamic range of 9.85 km (Fig. 2), considerably less than the global dynamic range for the Moon (19.9 km) or Mars (30 km) (*6*, *7*). Mercury contains numerous large impact structures (*8*, *9*) that influence the hemispheric shape but do not markedly affect the hypsometry.

Mercury's high bulk density, presumably the result of an iron-rich core that constitutes an unusually large mass fraction of the planet (*10*), yields a surface gravitational acceleration comparable to that of Mars for a body intermediate in size between Mars and the Moon. For at least some topography-producing forces, a higher gravitational acceleration results in less variation in elevation, which can account for the difference in topographic dynamic range between Mercury and the Moon. However, Mercury's shallow core-mantle boundary, at a depth of <400 km below the surface (*4*), could have affected viscous flow in Mercury's mantle and may have influenced the growth and relaxation of the largest structures (*11*). Shield-building volcanism and large-scale extension contribute substantially to the dynamic range of topography on Mars but have no evident counterparts on Mercury. Indeed,

[1]Department of Earth, Atmospheric and Planetary Sciences, Massachusetts Institute of Technology, Cambridge, MA 02139, USA. [2]Planetary Science Directorate, Southwest Research Institute, Boulder, CO 80302, USA. [3]Department of Terrestrial Magnetism, Carnegie Institution of Washington, Washington, DC 20015, USA. [4]NASA Goddard Space Flight Center, Greenbelt, MD 20771, USA. [5]Department of Earth, Environmental and Planetary Sciences, Case Western Reserve University, Cleveland, OH 44106, USA. [6]Department of Physics, University of California, Santa Barbara, CA 93106, USA. [7]Johns Hopkins University Applied Physics Laboratory, Laurel, MD 20723, USA. [8]Department of Geological Sciences, Brown University, Providence, RI 02912, USA. [9]Department of Earth and Ocean Sciences, University of British Columbia, Vancouver, BC V6T 1Z4, Canada. [10]Stinger Ghaffarian Technologies Inc., 7701 Greenbelt Road, Greenbelt, MD 20770, USA. [11]Department of Earth and Atmospheric Sciences, Purdue University, West Lafayette, IN 47907, USA. [12]Department of Earth and Space Sciences, University of California, Los Angeles, CA 90095, USA. [13]Institute of Planetary Research, German Aerospace Center, Berlin D-12489, Germany.

*To whom correspondence should be addressed. E-mail: zuber@mit.edu

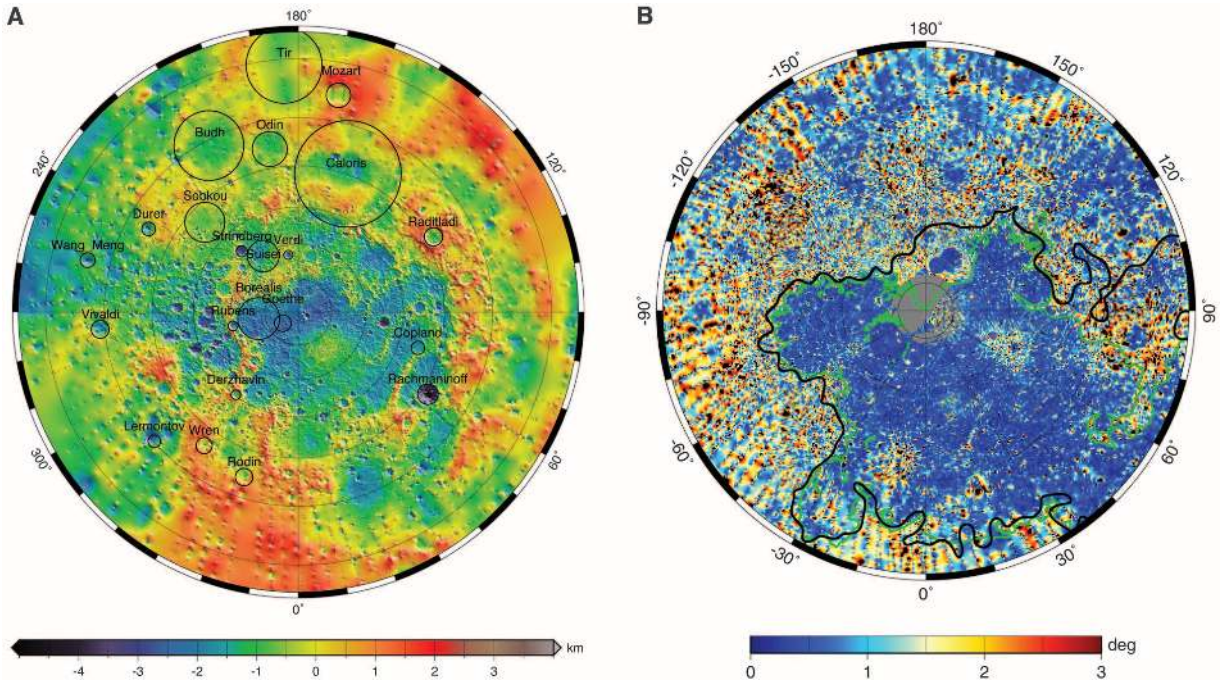

Fig. 1. (**A**) Polar stereographic projection of topography (local radius minus the radius of the HgM002 geoid, the gravitational equipotential referenced to the mean equatorial radius) (*4*) from the north pole to 5°S. The locations of selected major impact structures are shown as black circles. (**B**) Polar stereographic projection of median differential slope (*15*) on a baseline of length 3.2 km, from the north pole to 50°N latitude. The green line shows the mapped boundary of the northern smooth plains (*16*); the black line corresponds to the topographic contour of −1.24 km. Both maps include data collected through 24 October 2011.

if the topography associated with Tharsis and Valles Marineris is excluded, the dynamic range of the remaining topography on Mars can be approximated by the rim-to-floor depth of the Hellas basin. This figure is comparable to the dynamic range of topography on Mercury and is consistent with a gravitational influence on topographic relief for terrestrial planetary bodies.

A spherical harmonic fit of planetary shape (*12*) (table S1) confirms an elliptical form of the equator, with a long axis close to the prime meridian (*12*) (fig. S1), as well as an offset between the center of mass and center of figure in the equatorial plane (*5*, *13*). This distinctive feature of the planetary shape reflects a hemispheric difference in internal structure that could potentially arise from large-scale variations in crustal thickness or density, mantle density, or topography along Mercury's core-mantle boundary.

A north-polar projection of topography (Fig. 1A) shows irregular lowlands at high northern latitudes that are ~2 km deeper than the surrounding terrain. Portions of the boundary of the northern lowlands appear to follow segments of rims of degraded impact basins, but the large extent of the lowlands and the irregular shape of the remainder of the boundary suggest that additional processes were involved in the formation of relief. The northern lowlands are marked by a negative free-air gravity anomaly and are in a state of approximate local compensation (e.g., underlain by thinner than average crust) (*4*), although the area is likely not in strict local mass balance because of contributions to topographic support from flexural and membrane stresses. Barring some sort of offsetting structure near the south pole, the large area of low topography at high latitudes raises the prospect that the region may have migrated to the pole during a reorientation of the planet's principal inertia axes driven by the shallow mass deficit (*14*). If the present location of the northern lowlands is a consequence of polar wander, then the implied planet-scale reorientation must have occurred at a time when the outer portions of Mercury were sufficiently cool and mechanical-

Table 1. Geodetic parameters for Mercury derived from MLA topography.

Parameter	Value
Reference radius (km)	2440
North polar radius (km)*	2437.57 ± 0.01
Equatorial mean radius (km)†	2439.83 ± 0.05
Northern hemisphere mean radius (km)‡	2439.59 ± 0.05
Shape dynamic range (km)	9.848
Shape accuracy (m)	±25
High point (km)§ 11.222°N, 164.752°E	+4.024
Low points (km)§	
Rachmaninoff, 27.417°N, 57.215°E	−5.815
Polar crater, 85.446°N, 62.440°E	−5.824
Hypsometric mean (km)§	−0.589
Hypsometric median (km)§	−0.616
Hypsometric mode (km)§	−0.700
$(a - b)/a$ ‖	$(514 \pm 52) \times 10^{-6}$
ϕ_2 (°E)#	−18.6 ± 4
CoF-CoM *x* (km)**	0.133 ± 0.052
CoF-CoM *y* (km)**	0.193 ± 0.051

*Average of all MLA observations within 10° of north pole. †Average of all MLA observations within 15° of equator. ‡Mean planetary radius from a spherical harmonic least-squares fit to all observations with a Kaula constraint applied. §Relative to the reference radius. ‖*a* and *b* are, respectively, the semimajor and semiminor axes of the ellipse fit to shape measurements within 15° of the equator. #Longitude of the equatorial semimajor axis of the ellipse fit to near-equatorial shape. Longitude 0° coincides with one of the hot poles of Mercury, which is on the axis of minimum moment of inertia, and 90° on the equator is in the direction of the intermediate axis of inertia. **CoF-CoM is the offset of the center of figure (CoF) from the center of mass (CoM), the origin of the coordinate system for gravity and topography; *x* and *y* are the components of offset in Mercury's equatorial plane in the direction of 0° and 90°E, respectively.

ly strong to preserve a nonhydrostatic response to topographic stresses, as well as the present configuration of inertial axes.

A map of median differential slope (*15*) derived from the topographic measurements (Fig. 1B) illustrates that kilometer-scale slopes are generally much lower within the northern lowlands than in the surrounding areas. The lowlands are partially filled with a smooth plains unit that occupies more than 6% of Mercury's surface (*16*). On the basis of its geological characteristics, the plains have been interpreted as a product of flood volcanism early in Mercury's history marked by high rates of eruption of high-temperature lavas (*16*). Elemental composition measurements made with MESSENGER's X-Ray Spectrometer (XRS) indicate that the northern plains are similar in composition to basalts on other terrestrial bodies (*17*, *18*). The diameters of partially to fully buried craters on the plains unit imply that plains thicknesses, at least locally, exceed 1 to 2 km (*16*). The black curve in Fig. 1B shows that the boundary of the smoothed plains and of the area of low differential slope is reasonably well matched along a substantial portion of its length by a constant elevation relative to the geoid. These relationships suggest that the flood volcanism that created the northern plains involved highly fluid lavas.

At present, however, the northern smooth plains deviate from a level surface. In particular, the northern lowlands host a regional topographic rise (centered near 68°N, 33°E) that is ~950 km in diameter and is elevated by ~1.5 km above its surroundings. This northern rise is characterized by a large (~150 mGal) positive gravity anomaly (*4*). This value is only slightly less than the magnitude of the anomaly that would be predicted by topography alone and suggests at most limited compensation (e.g., by thickened crust) (*4*). The northern rise does not display kilometer-scale slopes distinguishable from the rest of the northern plains (Fig. 1B), and the size-frequency distributions of superposed impact craters indicate that the age of the rise surface is indistinguishable from that of the surrounding plains (*19*). Moreover, topographic profiles through volcanically buried craters on the rise indicate that the flooded floors tilt away from the highest point on the rise (*20*). These observations indicate collectively that at least a portion of the rise topography postdates the emplacement of the plains. The implied vertical motions following plains emplacement could be the result of lithospheric deformation, magmatic intrusion, or mantle dynamic uplift.

The Caloris basin (centered at 31°N, 160°E), 1550 km in diameter (*21*), is the best preserved and presumably youngest of the large impact basins on Mercury (*8*, *22*). A terrain model of the Caloris region derived from stereo images acquired during MESSENGER's first Mercury flyby (*23*) displayed basin-concentric rings and suggested long-wavelength undulations of the basin interior surface, but the lack of long-wavelength geodetic control in the model rendered these undulations uncertain. The MLA

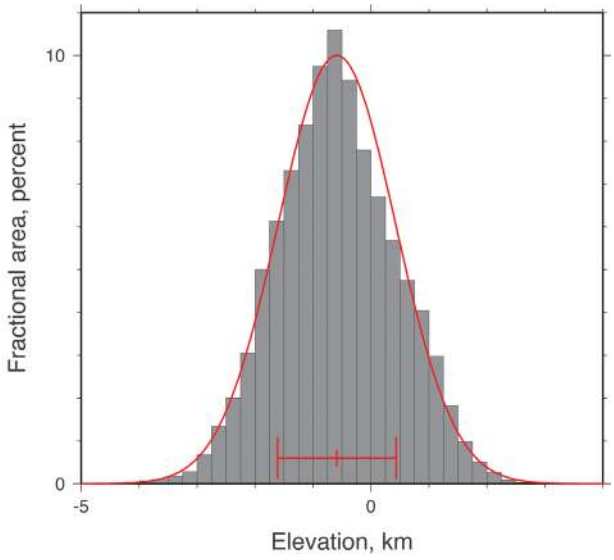

Fig. 2. Histogram of northern hemisphere elevations, relative to a sphere of radius 2440 km, projected onto an equal-area grid from 4°S to 83.5°N. The red line is a smooth curve fit to the observations; the red bar indicates ±1 standard deviation from the mean.

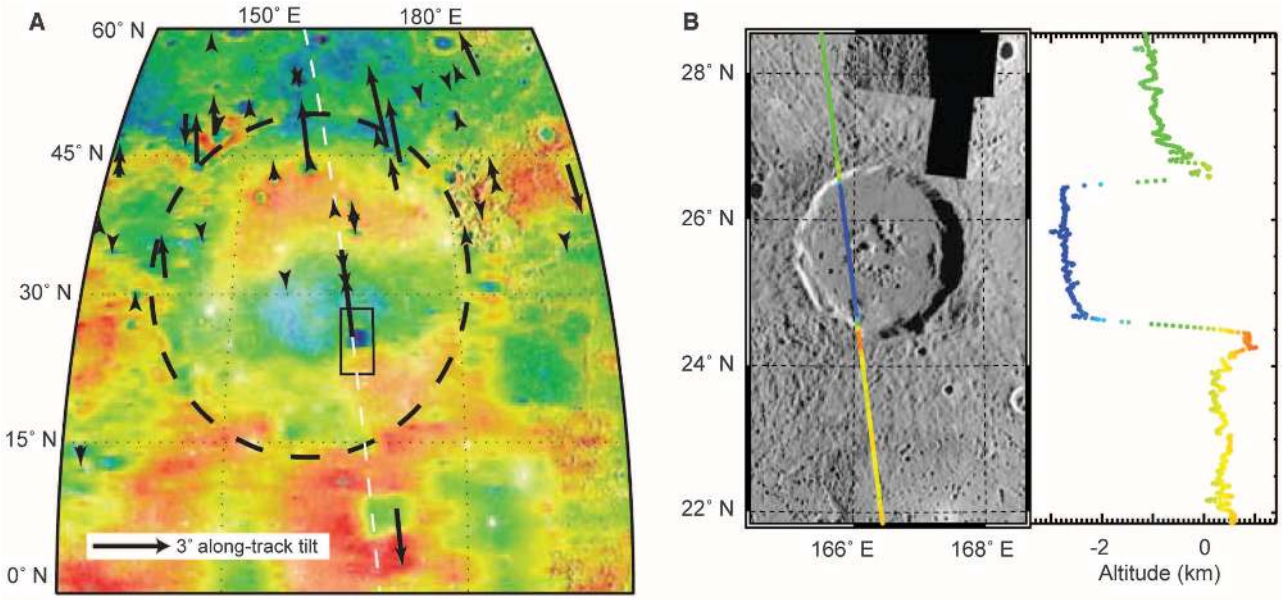

Fig. 3. (**A**) Average along-track tilts of the floors of impact craters (arrows) within and in the vicinity of the Caloris basin superimposed on regional topography. Tilts are obtained from representative MLA tracks across each crater and constitute the projection of total tilt onto the vertical plane containing the track. Arrow length is proportional to tilt. Dashed line shows the ground track of the profile in (B). (**B**) Profile MLASCIRDR1107292041 across the 100-km-diameter crater Atget demonstrates northward tilt of the crater floor.

topographic model, in contrast, is precisely controlled and enables confident characterization of long-wavelength topography. MLA observations confirm that the northern floor of Caloris is elevated relative to other parts of the basin interior, so much so that in places the floor lies above the basin rim (Fig. 3). This portion of the floor of Caloris appears to be part of a quasi-linear rise that trends generally west-southwest–east-northeast and extends over approximately half the circumference of Mercury at mid-latitudes (Fig. 1A). The floors of younger impact craters within and near Caloris (Fig. 3) display departures from the horizontal that generally correlate with regional tilts imparted by the long-wavelength topography of the region and are consistent with modification of Mercury's long-wavelength topography some time after the formation of Caloris and the emplacement of its interior and exterior volcanic plains.

The changes in long-wavelength topography within the Caloris basin and northern plains, and perhaps elsewhere on Mercury, occurred after both the end of heavy impact bombardment and the emplacement of the largest expanses of volcanic plains on the planet. One possible source of long-wavelength topography is the isostatic response to variations in crustal thickness. However, the oldest terrains on Mercury display crater size-frequency distributions at large crater diameters similar to those on the most densely cratered parts of the Moon (*24*). Thus, crustal formation substantially predated long-wavelength topographic change and cannot explain the observations. A second possible source of such long-wavelength change in topography is mantle convection (*25*). However, recent mantle convection simulations (*26*) constrained by internal structure models consistent with Mercury's long-wavelength gravity field (*4*) and by the latitudinal distribution of surface insolation do not produce surface deformation of the magnitude required to explain the observed topography. Another contribution to topographic change is volcanic and magmatic loading of the lithosphere along with its flexural response, which has a predictable pattern. Finally, long-wavelength changes in topography could be a deformational response to interior planetary cooling and contraction (*27*). Evidence for topographic changes during Mercury's evolution is consistent with evidence from the geometry of ridges and lobate scarps that these features accommodated surface strain over a substantial fraction of Mercury's geological history (*28*). Observations of the topography add to the growing body of evidence that Mercury was a tectonically, volcanically, and dynamically active planet for much of its evolution.

References and Notes

1. J. F. Cavanaugh *et al.*, *Space Sci. Rev.* **131**, 451 (2007).
2. S. C. Solomon, R. L. McNutt Jr., R. E. Gold, D. L. Domingue, *Space Sci. Rev.* **131**, 3 (2007).
3. The MLA is a time-of-flight laser rangefinder that uses direct detection and pulse-edge timing to determine precisely the range from the MESSENGER spacecraft to Mercury's surface. MLA's laser transmitter emits 5-ns-wide pulses at an 8-Hz rate with 20 mJ of energy at a wavelength of 1064 nm. Return echoes are collected by an array of four refractive telescopes and are detected with a single silicon avalanche photodiode detector. The timing of laser pulses is measured with a set of time-to-digital converters and counters and a crystal oscillator operating at a frequency that is monitored periodically from Earth.
4. D. E. Smith *et al.*, *Science* **336**, xxx (2012); 10.1126/science.1218809.
5. M. T. Zuber *et al.*, *Science* **321**, 77 (2008).
6. M. T. Zuber, D. E. Smith, F. G. Lemoine, G. A. Neumann, *Science* **266**, 1839 (1994).
7. D. E. Smith *et al.*, *Science* **284**, 1495 (1999).
8. P. D. Spudis, J. E. Guest, in *Mercury*, F. Vilas, C. R. Chapman, M. S. Matthews, Eds. (Univ. of Arizona Press, Tucson, AZ, 1988), pp. 118–164.
9. S. C. Solomon *et al.*, *Science* **321**, 59 (2008).
10. S. A. Hauck II, S. C. Solomon, D. A. Smith, *Geophys. Res. Lett.* **34**, L18201 (2007).
11. S. Zhong, M. T. Zuber, *J. Geophys. Res.* **105**, 4153 (2000).
12. See supplementary materials on *Science* Online.
13. D. E. Smith *et al.*, *Icarus* **209**, 88 (2010).
14. P. Goldreich, A. Toomre, *J. Geophys. Res.* **74**, 2555 (1969).
15. Median differential slope (*29*) removes the effect of larger-scale tilts from the elevation difference at a given baseline length. At each location x, half the difference in elevations between points one baseline length ahead and one behind along the altimetry ground track is subtracted from the difference in elevation between points one-half baseline length ahead and one-half behind, as $\tan\alpha = \{h[x + (l/2)] - h[x - (l/2)] - 0.5[h(x + l) - h(x - l)]\}/l$, where h is elevation, l is the baseline length, and α is the differential slope.
16. J. W. Head *et al.*, *Science* **333**, 1853 (2011).
17. L. R. Nittler *et al.*, *Science* **333**, 1847 (2011).
18. L. R. Nittler *et al.*, abstr. 142-3, paper presented at the Geological Society of America annual meeting, Minneapolis, 9 to 12 October 2011; http://gsa.confex.com/gsa/2011AM/finalprogram/abstract_193666.htm.
19. C. I. Fassett *et al.*, abstr. 142-6, paper presented at the Geological Society of America annual meeting, Minneapolis, 9 to 12 October 2011; http://gsa.confex.com/gsa/2011AM/finalprogram/abstract_196331.htm.
20. C. Klimczak *et al.*, abstr. 142-10, paper presented at the Geological Society of America annual meeting, Minneapolis, 9 to 12 October 2011; http://gsa.confex.com/gsa/2011AM/finalprogram/abstract_195048.htm.
21. S. L. Murchie *et al.*, *Science* **321**, 73 (2008).
22. J. W. Head *et al.*, *Space Sci. Rev.* **131**, 41 (2007).
23. J. Oberst *et al.*, *Icarus* **209**, 230 (2010).
24. C. I. Fassett, S. J. Kadish, J. W. Head, S. C. Solomon, R. G. Strom, *Geophys. Res. Lett.* **38**, L10202 (2011).
25. S. D. King, *Nat. Geosci.* **1**, 229 (2008).
26. N. Michel *et al.*, P41A-1581, paper presented at the American Geophysical Union fall meeting, San Francisco, 5 to 9 December 2011.
27. A. J. Dombard, S. A. Hauck II, S. C. Solomon, *Lunar Planet. Sci.* **32**, abstr. 2035 (2001).
28. M. T. Zuber *et al.*, *Icarus* **209**, 247 (2010).
29. M. A. Kreslavsky, J. W. Head III, *J. Geophys. Res.* **105**, 26695 (2000).

Acknowledgments: The MESSENGER project is supported by the NASA Discovery Program under contracts NAS5-97271 to the Johns Hopkins University Applied Physics Laboratory and NASW-00002 to the Carnegie Institution of Washington. We are grateful for the myriad contributions from the MLA instrument and MESSENGER spacecraft teams, and we appreciate three helpful reviews of an earlier version of the paper.

Supplementary Materials

www.sciencemag.org/cgi/content/full/science.1218805/DC1
Materials and Methods
Figs. S1 and S2
Table S1
Reference (*30*)

6 January 2012; accepted 2 March 2012
Published online 21 March 2012;
10.1126/science.1218805

ESCRT-III Governs the Aurora B–Mediated Abscission Checkpoint Through CHMP4C

Jeremy G. Carlton,* Anna Caballe, Monica Agromayor, Magdalena Kloc, Juan Martin-Serrano†

The endosomal sorting complex required for transport (ESCRT) machinery plays an evolutionarily conserved role in cytokinetic abscission, the final step of cell division where daughter cells are physically separated. Here, we show that charged multivesicular body (MVB) protein 4C (CHMP4C), a human ESCRT-III subunit, is involved in abscission timing. This function correlated with its differential spatiotemporal distribution during late stages of cytokinesis. Accordingly, CHMP4C functioned in the Aurora B–dependent abscission checkpoint to prevent both premature resolution of intercellular chromosome bridges and accumulation of DNA damage. CHMP4C engaged the chromosomal passenger complex (CPC) via interaction with Borealin, which suggested a model whereby CHMP4C inhibits abscission upon phosphorylation by Aurora B. Thus, the ESCRT machinery may protect against genetic damage by coordinating midbody resolution with the abscission checkpoint.

The final separation of daughter cells during cytokinesis is the ancestral function of the endosomal sorting complex required for transport (ESCRT) machinery (*1*–*5*) which also acts to resolve equivalent membrane scission events in multivesicular body (MVB) formation (*6*, *7*) and human immunodeficiency virus–1 (HIV-1) budding (*8*, *9*). Midbody recruitment of ESCRT-III, the filament-forming scission machinery, is an essential event in cytokinesis that is thought to provide constrictive force during abscission (*2*, *10*–*12*). An Aurora B–dependent